Talanta 282 (2025) 126990

Contents lists available at ScienceDirect

Talanta

journal homepage: www.elsevier.com/locate/talanta

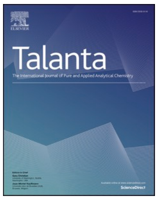

Highly stable scalable production of porous graphene-polydopamine nanocomposites for drug molecule sensing

Xiaohong Ding [a,b,c], Ruiqiang Chen [a], Jie Xu [a], Jiapeng Hu [a], Zhixuan Zhao [b], Cheng Zhang [d], Longhui Zheng [a], Huanyu Cheng [c,*], Zixiang Weng [b], Lixin Wu [b,**]

[a] *Fujian Provincial Key Laboratory of Eco-Industrial Green Technology, College of Ecological and Resources Engineering, Wuyi University, 354300, Wuyishan, China*
[b] *CAS Key Laboratory of Design and Assembly of Functional Nanostructures, Fujian Key Laboratory of Nanomaterials, Fujian Institute of Research on the Structure of Matter, Chinese Academy of Sciences, Fuzhou, 350002, China*
[c] *Department of Engineering Science and Mechanics, Materials Research Institute, Pennsylvania State University, University Park, PA, 16802, USA*
[d] *Fujian Key Laboratory of Functional Marine Sensing Materials, College of Material and Chemical Engineering, Minjiang University, Fuzhou, 350108, China*

ARTICLE INFO

Keywords:
Porous laser-induced graphene (LIG)
Controlled electropolymerization of polydopamine
Scalable and low-cost electrochemical sensors
Sensing of pharmaceutical molecules

ABSTRACT

As atenolol overdosing can lead to severe health complications, the rapid detection of atenolol intake in point-of-care settings is highly desirable. The recent advancement of redox analytical methodologies has facilitated the efficacious quantification of these compounds for drug analysis, but their performance still presents challenges in practical applications. This study addresses these challenges by controlling the electropolymerization of polydopamine (PDA) on highly porous laser-induced graphene (LIG) electrodes with enhanced electrochemical redox activity for the detection of drug molecules such as atenolol, with minimized interference with the other active substances to induce variation of electrochemical behavior. The enhanced sensitivity of atenolol is attributed to the superhydrophilicity and increased number of active surface sites and –NH_2 groups in the PDA polymer through a controlled polymerization process. Moreover, the simulation results further reveal that highly sensitive sensing of atenolol molecules relies on optimal adsorption of the atenolol molecule on dopamine or dopaminequinone structural units. The resulting sensors with high repeatability and reproducibility can achieve a low detection limit of 80 μM and a sensitivity of 0.020 ± 0.04 μA/μM within a linear range from 100 to 800 μM. The materials and surface chemistry in the electrode design based on highly porous LIG provide insights into the integration and application of future scalable and cost-effective electrochemical sensors for use in point-of-care or in-field applications.

1. Introduction

The large-scale production of sensing electrodes holds great importance in various fields, ranging from biomarker/drug detection [1–4] and healthcare/environmental monitoring [5–8] to industrial processes and consumer electronics [9]. Aside from metal electrodes, graphene exhibits high electrical conductivity, theoretical specific capacity, and specific surface capacitance, which emerges as a highly promising material for energy storage and electrochemical sensing electrodes [10–14]. However, the current high production costs, stringent requirements, and complex processes involved in the fabrication present challenges in practical industrial applications. The pursuit of large-scale, cost-effective products has brought porous laser-induced graphene (LIG) into the spotlight as a material of significant interest [15–20] due to its high electrical conductivity and biocompatibility. In drug development and point-of-care clinical treatment, the real-time monitoring of the concentration and activity of drug molecules is crucial for treatment evaluation. It is desirable to modify the LIG with polymers containing active functional groups to increase active site areas for enhanced sensitivity [21].

Catechol-containing molecules and polymers have been extensively applied to coat various materials such as metals, metal oxides, non-metal oxides, silica, ceramics, polymers, and nanomaterials to enhance interfacial interaction [22,23]. Among the catechol-containing coatings, polydopamine (PDA), inspired by mussels, provides an adhesive coating for cell immobilization or enhanced sensing performance due to the

---

* Corresponding author.
** Corresponding author.
E-mail addresses: huanyu.cheng@psu.edu (H. Cheng), lxwu@fjirsm.ac.cn (L. Wu).

https://doi.org/10.1016/j.talanta.2024.126990
Received 16 May 2024; Received in revised form 27 August 2024; Accepted 3 October 2024

plethora of functional groups [24,25]. Easily synthesized by exposing dopamine (3,4-dihydroxyphenylethylamine) to air in basic aqueous buffer solutions, a nanometer-thick, highly adhesive PDA coating can be produced on virtually any substrate [26]. The abundant catechol functionalities in PDA provide enhanced adhesion to both organic and inorganic surfaces via hydrogen bonds, coordination bonds, π-π stacking, coordination, or Michael addition processes [27]. Moreover, the catechol/quinone redox under electrochemical control provides a new possibility for sensing applications. For instance, the proton-coupled electron transfer reaction of catechol is linked to several biomolecular processes, such as the oxidation of NADH [28,29] and thiols [30], and in the neural signaling system [31]. While the function of catecholamines depends on how and to what extent they are oxidized [32], their controlled synthesis presents considerable challenges [33], especially on highly porous LIG substrates. Since the composition and changes of the structural units affect the performance of analytical electrodes due to the easy oxidation of catechol structures, it is of high significance to control them during the polymerization process.

As an organic semiconductor, PDA can continuously grow in layer thickness beyond the complete coverage of the substrate. Unlike autoxidation, electro-polymerization that occurs at the solution/electrode interface can achieve controlled and selective deposition of polydopamine layers [34]. Besides offering high spatial control and selectivity in electro-polymerization, the electro-oxidation of dopamine on various electrode materials or under varying conditions can be explored to further enhance the control over polymerization. Improved dopamine sensing (e.g., a fourfold increase in sensitivity and a fivefold decrease in detection limit) is achieved after coating boron-doped carbon nanowalls with PDA/polyzwitterion due to facilitated dopamine transport and oxidation [35]. The combination of PDA with reduced graphene oxide in the composites also allows for enhanced sensing of uranium [36] and free chlorine [37].

Herein, this study integrates highly porous LIG with physicochemical PDA thin films for the detection of non-redox drug molecules. The composition of PDA is first fine-tuned and incorporated into the polymer chains on the highly porous LIG through a controllable electro-polymerization process. After controlled electropolymerization to optimize the properties, the porous LIG-PDA sensing electrodes are exploited to detect the atenolol absorbed onto the electrode surface in a proof-of-concept demonstration. The PDA-induced superhydrophilicity together with enhanced active surface sites from the controlled polymerization process contributes to the increased sensitivity of atenolol. Additionally, a high –NH_2 content in the PDA polymer chain significantly enhances the sensitivity of the sensor to detect atenolol molecules with a low limit of detection of 80 μM. Computational analysis further confirms that an increased presence of DA or DHI units in the PDA structure provides optimized adsorption of atenolol molecules on DA/DQ structural units, culminating in improved sensing performance. The efficient and cost-effective diagnostic approach presented in this work holds promising potential for delivering personalized medicine.

2. Materials and methods

2.1. Materials

The polyimide film (005” Kapton) with a thickness of 75 μm was purchased from CS Hyde Company (product no. 18-5S-1-36). Dopamine hydrochloride (DA, product no. D103111) and atenolol (product no. A124776) were obtained from Aladdin. All materials and reagents were used without further purification. The phosphate buffer saline (PBS, 0.1 M, pH of 7.2) was acquired from Sangon Biotech (Shanghai, China). Deionized water was provided by a ULUPURE purification system (UPT-I-5T, Youpu, Sichuan, China). The adapter from Changsha SINJEEN electronic technology Co., Ltd. provided a connection between the electrodes and the data acquisition system for *in vitro* tests.

2.2. Fabrication of LIG electrodes

The CO_2 laser (Universal Laser Systems, laser cutter VLS3.50) was used to scribe the polyimide thin film to yield the porous LIG electrode patterns with a diameter of 2 mm under ambient conditions. The laser parameters were optimized for the speed (0–28 cm/s) and the power (0–35 W) of the laser while the pulses per inch (PPI) were set to 1000. While the pristine LIG was directly used as the counter electrodes, the LIG was further modified with Ag/AgCl ink and PDA to serve as the reference and working electrodes. The conductive LIG on a glass substrate was connected to the adapter, with the excessive area covered by a PI tape to avoid interference with analytes (Fig. S1).

2.3. Electro-polymerization of DA on LIG electrodes

Polydopamine with a concentration of 5 mM DA in phosphate buffer (1.0 mM, pH 7.2) was polymerized on the LIG electrodes. The polymerization reaction was initiated by cyclic voltammetry (CV) [38] between −0.5 and + 0.5 V. The samples polymerized for 10, 15, and 20 cycles were denoted as LIG-PDA-10, LIG-PDA-15, and LIG-PDA-20.

2.4. Characterization

A Raman spectrometer with a blue laser at 532 nm (Labram HR Evolution Raman Spectrometer system) and an X-ray diffractometer (PANalytical, model Empyrean) was used to characterize the resulting LIG electrodes. Scanning electron microscopy (SEM) was performed using a JCM 6000 instrument manufactured by JEOL (Hitachi High-Technology Co., Ltd., Japan). Attenuated total reflectance fourier transform infrared spectroscopy (ATR-FTIR, Thermo Scientific iN10) analysis was conducted in the range of 400–4000 cm^{-1}.

2.5. Electrochemical characterization

Cyclic voltammetry (CV) was employed to determine the electroactive surface area of the LIG and PDA-modified LIG electrodes in 5×10^{-3} M $[Fe(CN)_6]^{3-/4-}$ in 0.1 M PBS (pH 7.2) buffer solution. Electrochemical Impedance Spectroscopy (EIS) was also performed in 0.1 M PBS (pH 7.2) to analyze the kinetic process on the electrode interface.

2.6. Electrochemical sensing of atenolol

The standard solution of 1.0 mM atenolol solution was prepared by dissolving 0.67 mg of atenolol in the Britton-Robinson (BR, pH = 10) and further diluting with the buffer for varying concentrations from 100 to 800 μM. The *in vitro* sensing was performed by CV measurements. All electrodes were thoroughly rinsed with ethanol and ultra-purified water before testing to avoid surface contamination.

2.7. Computational details

The geometries of atenolol, DA, LDC, DHI, DQ, DC, IQ molecules, and dimers were first optimized by density functional theory (DFT) at the B3LYP-D3(BJ)/6-31G** level. Based on the optimized geometries, the binding energies were calculated at the DFT-B3LYP-D3(BJ)/6-311+G** level. All the DFT calculations were performed with the Gaussian 16 package [39]. The electrostatic surface potentials (ESP) were calculated using the Multiwfn program [40].

3. Results and discussion

3.1. Synthesis and structure of porous LIG-PDA nanocomposite electrodes

The fabrication of the electrodes based on LIG and its nanocomposite starts with a versatile CO_2 laser processing step to convert the PI sheet into black carbonaceous materials (Fig. 1a). The active working

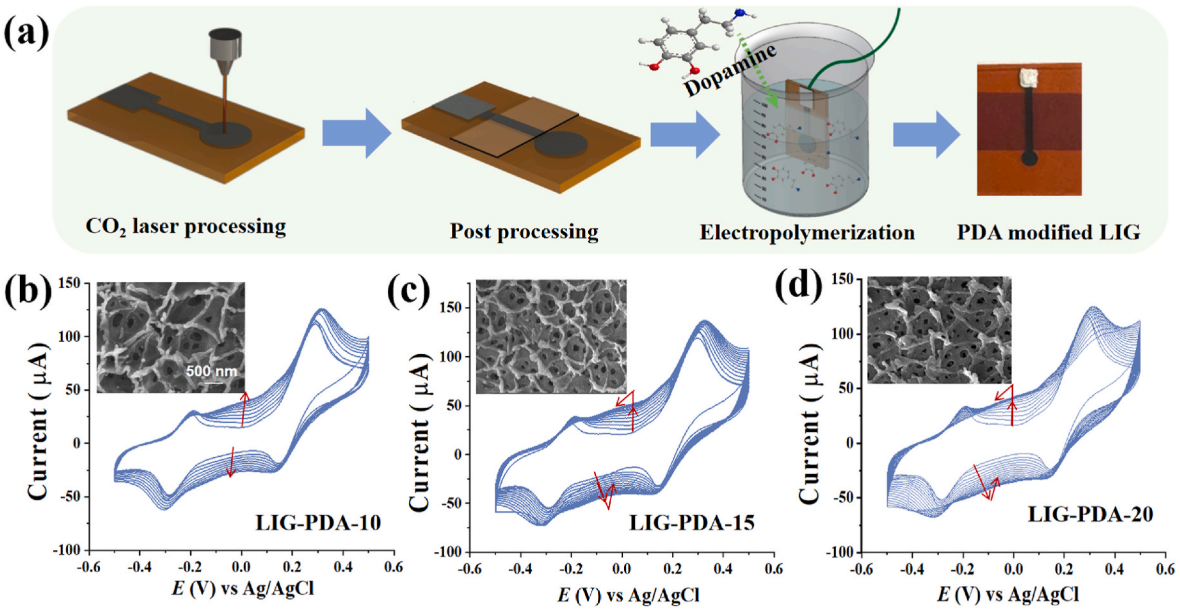

Fig. 1. An overview of (a) Schematic showing the fabrication process of the integrated porous laser-induced graphene (LIG) and its nanocomposite with polydopamine (PDA) from electro-deposition on the polyimide (PI) film as patterned electrodes for drug sensing and treatment evaluation. The straight conductive line was encapsulated with Kapton tape for minimized interference. CV curves at the (a) 10th, (b) 15th and (c) 20th cycles in 5 mM DA PBS solution (0.1 M) at 50 mV s^{-1}. The arrows indicates the change in the current peak as the polymerization cycle number increases, with SEM images shown in the insets.

electrode with a diameter of 2.0 mm is configured into a three-electrode setup for the electrodeposition of the PDA film. Rich in DA with dangling amine groups, PDA can facilitate hydrogen electro-absorption. Several reactions involved in the PDA polymerization produce six typical compounds, namely: dopamine (DA), dopaminequinone (DQ), leukodopaminechrome (LDC), dopaminechrome (DC), dihydroxyindole (DHI), and indolequinone (IQ) [41]. All of these compounds can potentially be incorporated into polymeric PDA via covalent bonds [42].

The electro-polymerization of PDA on the porous LIG electrodes in a 0.1 M PBS buffer (pH 7.2) containing 5 mM dopamine is revealed by the CV curves of the resulting electrodes. As deposition increases from 1 to 30 cycles during consecutive electropolymerization, two redox couples appear in polymerization cycles with noticeable variations in peak shifts, and the corresponding current density changes from 114 to 51 μA (Fig. 1b, c, d) due to changes in the depositing substrates [43]. The current peak at 0.32 V reaches its maximum at 10 cycles, followed by a gradual decrease until disappearance, which indicates the completion of the redox reaction for the DA electrodeposition and the complete consumption of DA in the solution [25,34,37]. Specifically, the oxidation peaks at 0.32 V and −0.19 V during the first cycle result from the oxidation of DA to DQ and then the DQ oxidation, whereas the two reduction peaks at 0.13 V and −0.30 V correspond to the reduction of DQ and DC, respectively. The increase in the cycle number also results in the increase of the current density in the redox peak utill 15 cycles, followed by a diminishment. These results validate the successful electropolymerization of PDA on the porous LIG electrodes.

The morphological changes of the porous LIG nanocomposite electrodes reveal that the PDA deposition often begins at the sharp edges (insets in Fig. 1b, c, d). The pristine LIG features interconnected micro-nano pores (Fig. S2) and sharp edges with 97.73 mol% C and 2.27 mol% O atoms (Table S1). The clear deposition of PDA at the sharp edges in LIG-PDA-10 expands to gradually reduce the porous LIG structures, as deposition increases to 15 and 20 cycles. The increase in the N atoms from 1.89 to 3.57 mol% also indicates the increased content of PDA film (Fig. S3). Besides nitrogen, a significantly increased content of oxygen from 2.27 mol% in LIG to 9.17/6.73/8.91 mol% for LIG-PDA-10/15/20 is also observed, which indicates the incorporation of catechol. As a result, electropolymerization can provide the porous LIG-PDA electrode with controllable morphological and chemical constitution changes.

Characterization of the porous LIG-PDA nanocomposite electrodes with ATR further reveals the chemical structure. A broad band spanning from 3200 to 3700 cm^{-1}, indicative of –OH stretch vibrations adsorbed on the LIG surface enhances, suggests successful deposition of the PDA layer (Fig. 2a). Peaks emerging in the 2800-3000 cm^{-1} region are ascribed to the C–H bonds present in the polydopamine or dopamine units, since the PDA macromolecular chains contain benzene rings, phenolic hydroxyl groups, and amido groups [44]. The peaks at 1315 cm^{-1} and 1429 cm^{-1} are attributed to the N–H shearing vibration of the amide group and the C–O vibration. The peak at 1653 cm^{-1} is assigned to the stretching vibration of the aromatic ring and the bending vibration of N–H, whereas the adsorption band at 3338 cm^{-1} belongs to the stretching vibration of phenolic O–H and N–H. These signature bands indicate successful anchoring of PDA on the LIG surface.

With a green laser at 532 nm to perform the Raman spectroscopic characterization of LIG, two prominent peaks at 1329 and 1583 cm^{-1} are distinctly observed in LIG to correspond to the D and G bands, respectively (Fig. 2b). The G band is emblematic of graphene structures, indicative of sp^2 hybridized carbon atoms in a two-dimensional hexagonal lattice, whereas the D band is attributed to defects or edges within the graphene lattice. A lower density of defects in graphene contributes to superior electronic properties such as electrical conductivity and carrier mobility. Following the DA polymerization, the I_D/I_G intensity ratio of the porous LIG-PDA nanocomposite decreases from 1.09 (LIG) to 0.97/0.84/0.73 (LIG-PDA-10/15/20), likely resulting from the passivation of the defects [45,46] and a reduction reaction on the LIG [37]. The interaction between PDA and LIG influences the π-π interactions between the graphene layers, which can also change the electronic transport properties of the resulting nanocomposite [25,37,47,48]. Furthermore, the water contact angle decreases from 83° for pristine LIG to 0° for PDA-modified LIG electrodes. The resulting superhydrophilicity (as demonstrated in Video S1) is attributed to the increased –OH and –NH$_2$ polar functional groups (to increase surface energy and thus the wettability) in the PDA that binds strongly on the LIG surface via the catechol groups within the PDA structure. Superhydrophilicity helps consistently and reliably increase the contact between the sample solution and sensor surface for enhanced sensitivity and reliability.

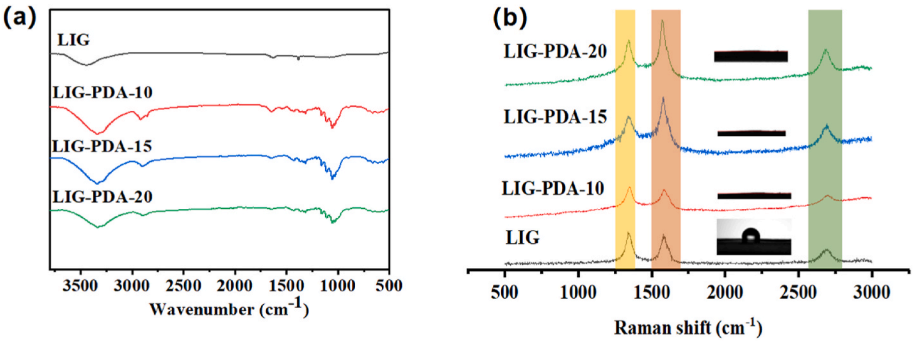

Fig. 2. (a) Attenuated total reflectance flourier transform infrared spectroscopy (ATR-FTIR) spectra and (b) Raman spectra of the porous LIG and LIG-PDA nanocomposite electrodes, with the water contact angle shown in the insets.

Compared with the pristine LIG (Fig. 3), the porous LIG-PDA nanocomposite electrodes exhibit an obvious increase in the O and N atoms in the XPS results (Table S2), indicating an altered electronic environment in the LIG from PDA deposition. The highest π-π* shakeup of 289.56 eV in PDA modifed LIG significantly enhances the stability of the binding between PDA and LIG for long-term stable device performance. The polymerization of PDA may involve six different structural units (DA, DQ, LDC, DC, DHI, and IQ) incorporated into the molecular chain [34, 48]. The N1s peak of LIG-PDA-15 in the XPS shows 61.54 and 16.73 mol % of N in the form of C–N (399.04 eV) and C–NH_2 (401.70 eV), respectively. The highest C–NH_2/C–N ratio of 0.27 indicates the main structural units of DA and DQ due to their high C–NH_2 content. The C–NH_2/C–N ratio of 0.19/0.20 in LIG-PDA-10/20 further narrows down the main structural units to LDA or DHI due to the amino cyclization. The highest C–NH_2 content in LIG-PDA-15 suggests the highest content of primary amine structures in the PDA polymer [47,48].

3.2. *Electrochemical property of the porous LIG-PDA nanocomposite electrodes*

Cyclic voltammetry at different scan rates in PBS determines the kinetic process and electroactive surface area of LIG and LIG-PDA electrodes (Fig. 4). Besides $[Fe(CN)_6]^{3-}/^{4-}$ redox couples observed at 0.25 V and 0.17 V in LIG and LIG-PDA electrodes (Fig. 5a–d), the linear fit between the log oxidation peak current and the log scan rate gives a slope of 0.53 for LIG to indicate a diffusion-controlled redox process [49, 50]. Different from the slopes of 0.55/0.52 for LIG-PDA-10/15 electrodes with a diffusion-controlled redox process, the larger slope of 0.60 for the LIG-PDA-20 indicates the combined diffusion and adsorption at the interface [49]. The well-maintained porous structure after PDA deposition confirmed by XPS and SEM is beneficial to the diffusion-controlled process. The C–OH in PDA contributes more to the adsorption process, whereas the C–NH_2 favors the diffusion-controlled process.

The comparison of CVs in $[Fe(CN)_6]^{3-/4-}$ shows that the PDA modified LIG has larger redox peaks than the pristine LIG (Fig. 5e). The maximum peak in LIG-PDA-15 features a notable faradaic current couple of 92.20 μA and −75.78 μA at 100 mV s^{-1}. Similarly, LIG-PDA-15 also exhibits a significantly increased capacitive current in the BR buffer (Fig. 5f), which correlates with improved electrochemical sensing.

The Randles–Sevcik equation [49] describes the electrochemical behavior of $[Fe(CN)_6]^{3-}$:

$$I_p = 2.69 \times 10^5 \times A\, D^{1/2}\, n^{3/2}\, v^{½}\, c, \tag{1}$$

where I_p is the oxidation peak current (A), A is the electrode real area (cm^2), D is the diffusion coefficient of the redox molecules in solution (7.26×10^{-6} cm^2 s^{-1} for $K_3[Fe(CN)_6]/K_4[Fe(CN)_6]$) [51], $n = 1$ is the number of electrons participating in the reaction, $c = 5 \times 10^{-3}$ M is the concentration of the redox molecules, and v is the scan rate (V s^{-1}). Therefore, the increased slope for the LIG-PDA over LIG (Table S3) is attributed to the increased active electrode surface area. The electrochemically active surface area of 0.067 and 0.159/0.225/0.134 cm^2 for LIG and LIG-PDA-10/15/20 reveals that the active surface area of the LIG modified with 15 PDA deposition cycles is about 3.4 times that of pristine LIG.

After performing electrochemical impedance spectroscopy (EIS) in 5 $\times$ 10^{-3} M $[Fe(CN)_6]^{3-/4-}$ within a 0.1 M PBS buffer solution (pH 7.2), the fitting of the Nyquist plots (Fig. 6) gives the solution resistance in the range of 113.9–156.8 Ω for pristine LIG and LIG-PDA-10/15/20 (Table S4). A distinct semicircle in the high-frequency region suggests a process governed by both diffusion- and charge transfer-controlled electrochemical behavior. The charge transfer resistance decreases from 934.9 Ω for the pristine LIG to 775.2 Ω and 848.1 Ω after 10 and 15 polydopamine deposition cycles, respectively (Table S4). To provide insight into the characteristics of the diffusion-controlled processes, the Warburg impedance is reduced by factors ranging from 4 to 9 from pristine LIG to all PDA modified LIG, substantiating the role of PDA in facilitating ion diffusion. Additionally, the constant phase element (CPE1) values decrease from 0.93529 for the pristine LIG (which closely approximates an ideal capacitor) as the number of the deposition cycle increases. The significant decrease in the charge transfer resistance and Warburg impedance demonstrates effective charge transfer at LIG-PDA surfaces.

3.3. *Sensing performance of the porous LIG-PDA nanocomposite sensor for atenolol*

The absorption of atenolol on and interaction with PDA can influence the electrochemical behavior of the electrode for the potentially sensitive detection. As the pH value influences the oxidation activity of atenolol, the electrochemical behaviors of 400 μM atenolol in the BR solution are studied as a function of pH (5, 7.5 and 10) at a scan rate of 0.05 V s^{-1} (Fig. S4). Due to the protonation of the amino group in atenolol [52], there is no electrochemical response at a pH of 5 and 7. In contrast, there is a clear oxidation peak at 0.75 V at pH of 10. The sensitivity comparation of these electrodes to 400 μM atenolol shows the largest peak current value (29.8 μA) for LIG-PDA-15 over the pristine LIG (7.4 μA) and LIG-PDA-10/20 (21.92/12.56 μA) due to the largest active sites. The CV scans using LIG-PDA-15 at a scan rate of 0.05 V s^{-1} show that the peak current increases from 26.26 to 40.82 μA as the atenolol concentration increases from 100 to 800 μM (Fig. 6a). Meanwhile, the peak current potential shifts to a higher value, which is attributed to the adsorption effect of the atenolol on PDA. The linear fit between the current response and the atenolol concentration gives: I (μA) = 0.020 C (μM) +23.43 (R^2 = 0.970), which gives a sensitivity of 0.020 ± 0.04 μA/μM that is about three times higher than the pristine LIG (0.0069 ± 0.04 μA/μM). However, the sensitivity is reduced to 0.0120 ± 0.002 μA/μM (Fig. S6) when integrated into the three-electrode configuration (Fig. 6b, inset), which is likely attributed

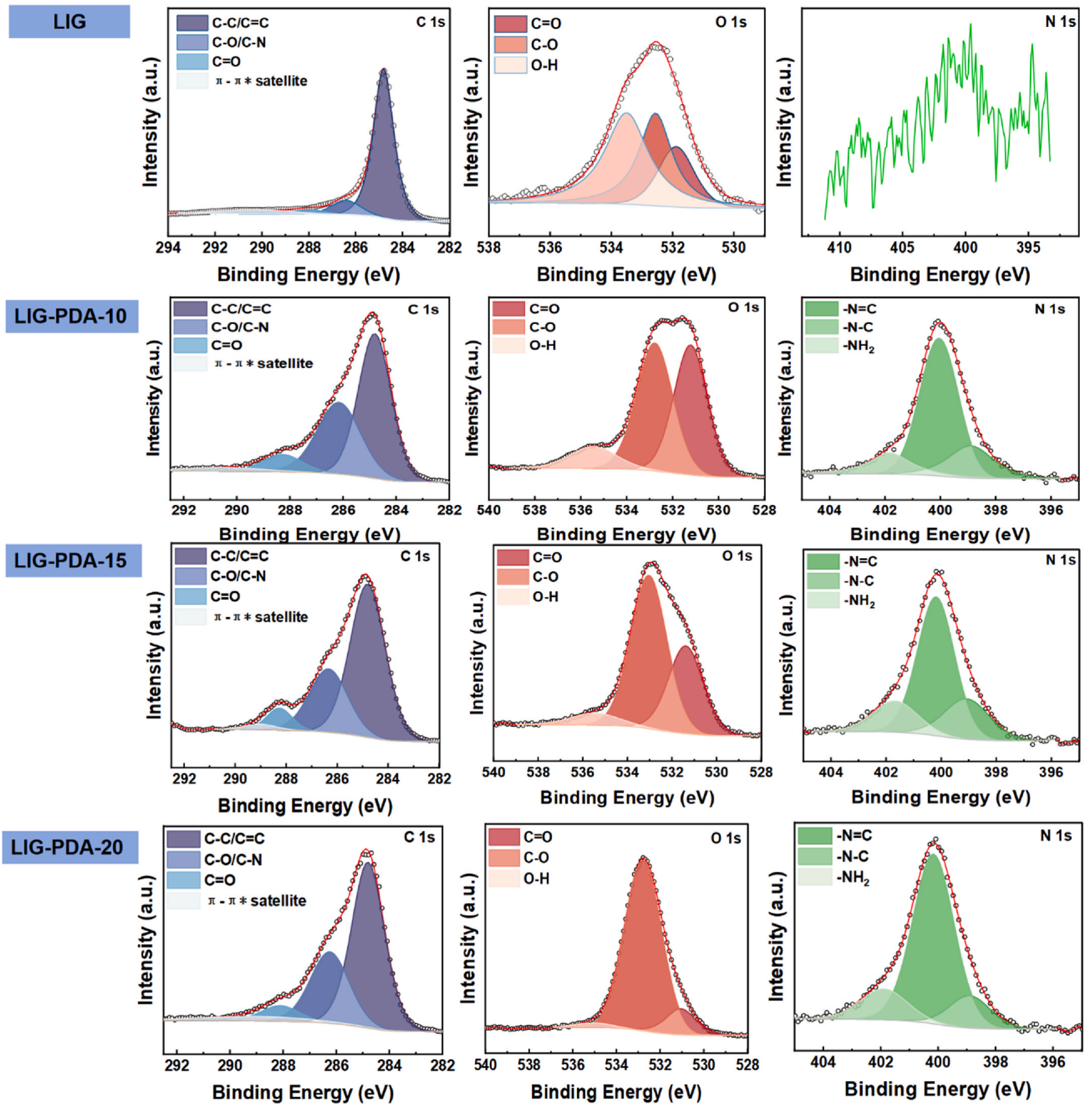

Fig. 3. High-resolution XPS spectra of the porous LIG and LIG-PDA nanocomposite electrodes with 10, 15, and 20 deposition cycles in the C, O, and N energy regions.

to the increased impedance from the connecting LIG line. The limit of detection (LOD) is further determined as 80 μM by using $LOD = 3\sigma/s$, where s represents the sensitivity and the standard deviation of the response ($\sigma = 0.538$) is obtained from five repeated measurements with the LIG-PDA-15 in BR buffer. Compared with the other sensors previously reported in the literature, the sensor based on the PDA-modified porous LIG exhibits high sensitivity, reproducibility, scalability, and facile integration (Table S5).

Three repeated CV measurements of 400 μM atenolol with the LIG-PDA-15 electrode reveal good repeatability, with the relative standard deviation (RSD) of 0.208 (Fig. S7a). Additionally, three LIG-PDA-15 electrodes manufactured independently also give a negligibly small RSD of 1.36 (Fig. S7b), indicating excellent reproducibility. As propranolol and nifedipine are usually found together with atenolol in the same medicine, they are chosen as interfering substances in this study. While propranolol exhibits a peak current at 1.03 V, there is no obvious peak from nifedipine (Fig. S8a). As propranolol (or nifedipine) of 400 μM is added into the atenolol solution of 0.4 mM (Fig. S8b), the peak current at 0.85 V (the peak of atenolol) is decreased from 29.8 μA to 22.5 μA (or) 17.3 μA by 24.5 % (or 41.9 %). The selectivity of the sensor toward atenolol can be further improved with differential pulse voltammetry (DPV) and square-wave voltammetry (SWV) [53,54].

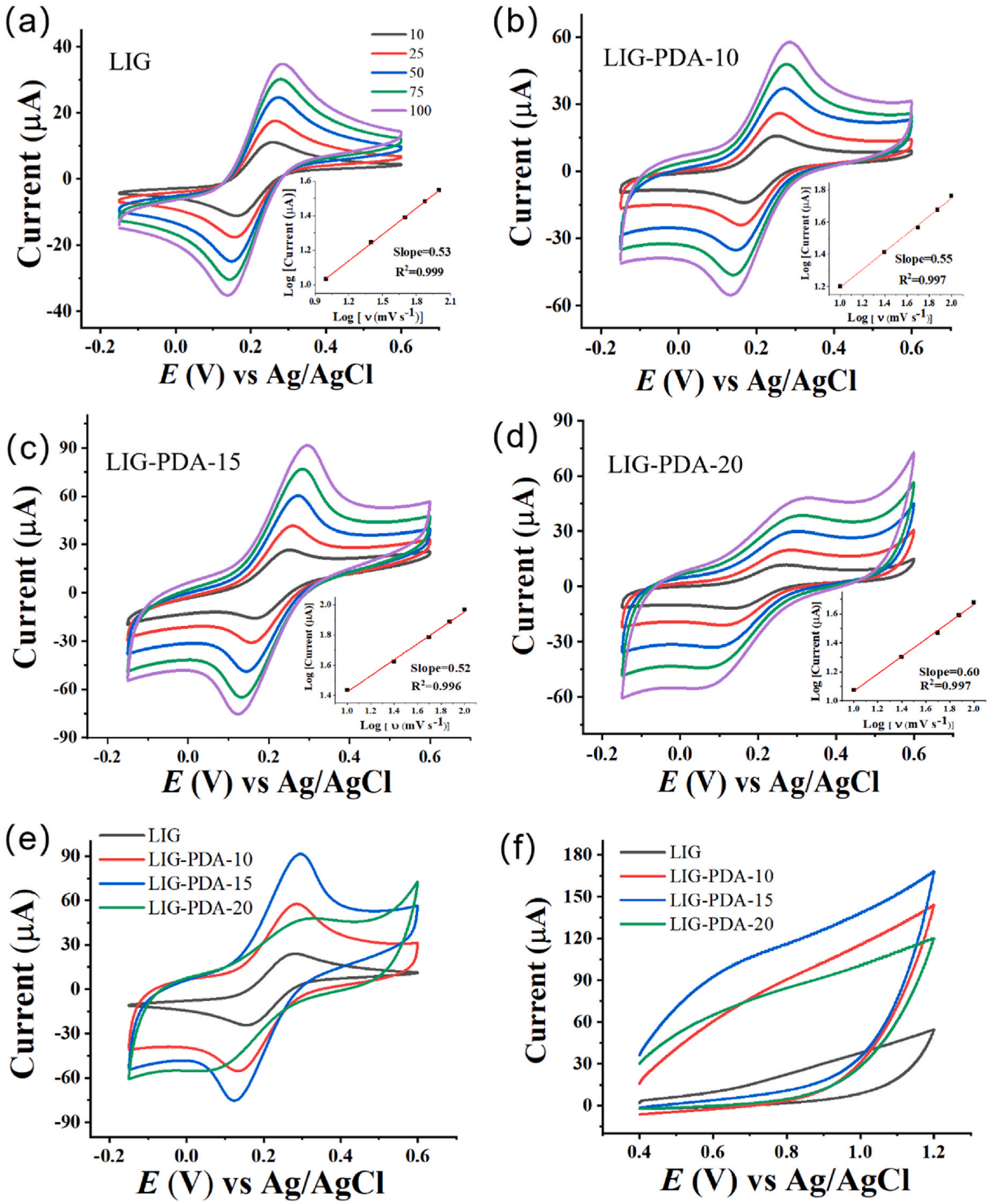

Fig. 4. CV curves of (a) pristine LIG, (b) LIG-PDA-10, (c) LIG-PDA-15, (d) LIG-PDA-20 at various scan rate (10, 25, 50, 75, and 100 mV s^{-1}) in 5 × 10^{-3} M [Fe(CN)6]$^{3-/4-}$ in PBS buffer solution (pH 7.2), with the log oxidation peak currents versus the log scan rate (ν) shown in the insets. Comparison in the CV curves between LIG and LIG modified with PDA in (e) 5 × 10^{-3} M [Fe(CN)$_6$]$^{3-/4-}$ and (f) Britton-Robinson (BR) solution (pH = 10) at a scan rate of 100 mV s^{-1}.

3.4. Intermolecular interaction between PDA and atenolol

The interaction between PDA and atenolol molecules can be investigated by calculating the binding energy, with the optimal conformations of molecular structures (Fig. 7). Compared to keto-dopamine, hydroxy-dopamine exhibits a more dispersed electron cloud distribution. Although the electronegativity of the oxygen atoms is the same, the hydrogen atom in the hydroxy group can offset some of the electronegativity of the oxygen atom resulting in a weak electron-withdrawing group. In contrast, no other atoms in the keto group can balance the electronegativity of the oxygen atom, so the substituent almost entirely reflects the electronegativity of oxygen and acts as a strong electron-withdrawing group. Compared to DA/DQ and LDC/DC, DHI/IQ have extended conjugation lengths, leading to more delocalized electrons and, thus, a more dispersed electrostatic potential (ESP) distribution. For the atenolol molecule, the central aromatic ring and the atoms directly connected to the aromatic ring are negatively charged, with the side chains on both sides being positively charged.

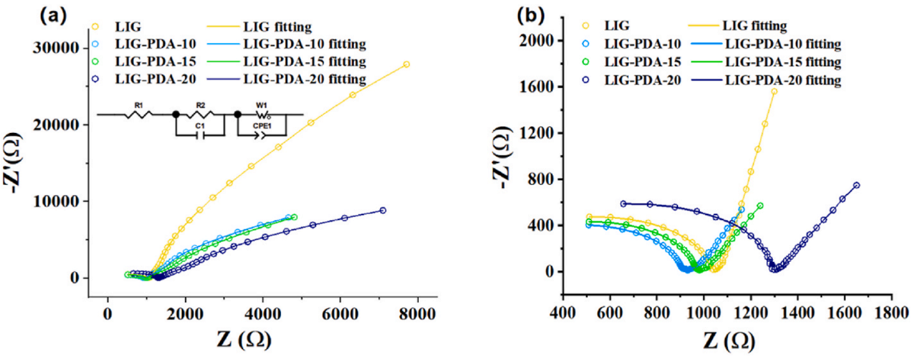

Fig. 5. (a) EIS plots of LIG and PDA-modified LIG electrodes, with the equivalent circuit model shown in the inset. (b) Enlarged EIS spectra in the high frequency region.

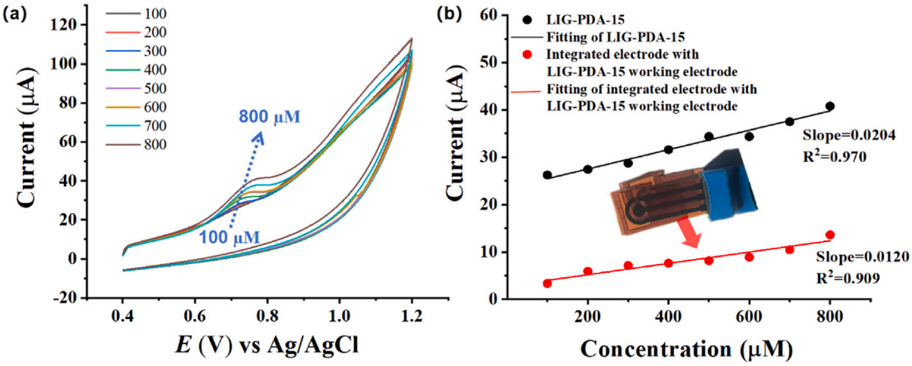

Fig. 6. (a) CV of LIG-PDA-15 in various atenolol concentrations from 100 to 800 μM in BR solution (pH 10.0) and (b) the calibration curve of atenolol calculated by the peak currrent as a function of atenolol concentration.

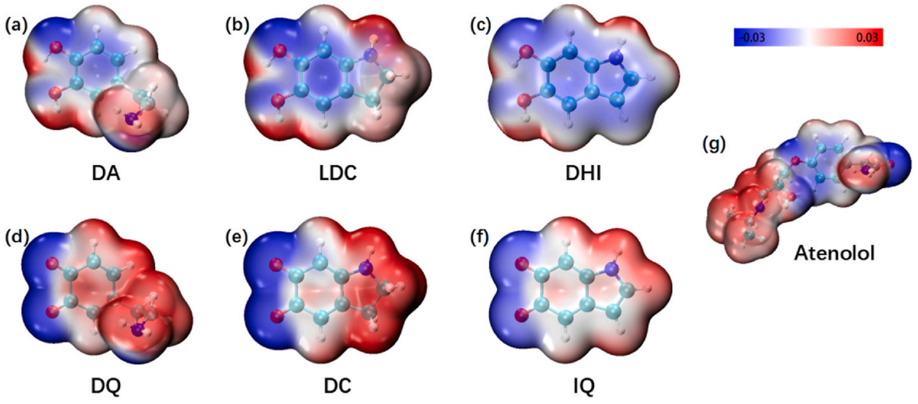

Fig. 7. ESP diagrams of the optimized geometric structures of (a–f) DA, LDC, DHI, DQ, DC, IG and (g) atenolol molecules. In these diagrams, white, cyan, blue, and red spheres represent H, C, N, and O atoms, respectively. The color gradient from blue to white to red represents the change in values from negative to positive.

Molecular pairs formed between areas of opposite electronegativity exhibit strong intermolecular forces, so the binding energies in 13 atenolol-dopamine molecular pairs are calculated and compared. A more negative value of the binding energy suggests a stronger interaction between the molecules. The six most stable binding modes formed between the atenolol and dopamine molecules (Fig. 8) follow the order of interaction strength: DHI > DA > IQ > DC > DQ ≥ LDC (Table S6). There is a strong π-π* interaction and hydrogen bonding between DHI and atenolol molecules, numerous hydrogen bonds between DA and atenolol molecules, and a strong π-π interaction between IQ and atenolol molecules. In contrast, the other three molecules (DC, DQ, and LDC) only form weaker π-π* interactions or hydrogen bonds with atenolol molecules. This result indicated that the increased –NH_2 content mainly from DA and DQ structural units in PDA (highest in LIG-PDA-15) provides enhanced adsorption and electrochemical sensitivity of atenolol on the electrode. However, excessively large adsorption due to π-π* interactions and hydrogen bonding may lead to reduced sensitivity.

4. Conclusion

In summary, this work reports the design, characterization, and application of the porous LIG-PDA nanocomposite electrodes for the detection of drugs at trace concentrations. Besides modulating the catechol content to improve superhydrophilicity, incorporating more DA and/or DQ units could also lead to optimized adsorption of atenolol molecules on PDA. With a 3.4 times larger surface active site than

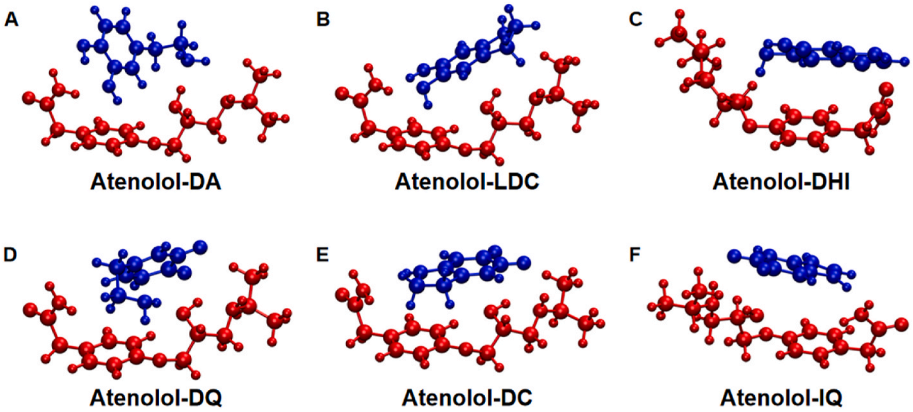

Fig. 8. Optimal stacking configurations of different dopamine molecules (blue) with atenolol (red).

pristine LIG, the 3D porous superhydrophilic LIG-PDA electrodes provide the resulting sensor with a low LOD of 80 μM and a sensitivity of 0.020 ± 0.04 μA/μM for atenolol detection. The mechanism study of the interfacial interaction at the molecular level also reveals the impact of surface chemistry on sensor performance. The increased content of $–NH_2$ in the constitutional units enhances the electrochemical sensing performance of LIG-PDA electrodes. Furthermore, the π-π* interactions and hydrogen bonding between atenolol and the LIG-PDA electrodes are the primary reasons for the variation in sensing signals.

CRediT authorship contribution statement

Xiaohong Ding: Writing – original draft, Methodology, Investigation, Funding acquisition, Formal analysis, Data curation, Conceptualization. **Ruiqiang Chen:** Validation, Methodology. **Jie Xu:** Resources. **Jiapeng Hu:** Funding acquisition. **Zhixuan Zhao:** Data curation. **Cheng Zhang:** Data curation, Conceptualization. **Longhui Zheng:** Project administration, Methodology, Investigation. **Huanyu Cheng:** Writing – review & editing, Supervision, Funding acquisition, Formal analysis, Data curation, Conceptualization. **Zixiang Weng:** Writing – review & editing, Investigation, Data curation. **Lixin Wu:** Supervision, Resources, Project administration, Investigation, Funding acquisition, Conceptualization.

Declaration of competing interest

The authors declare that they have no known competing financial interests or personal relationships that could have appeared to influence the work reported in this paper.

Acknowledgment

This work is supported by the Natural Science Foundation of Fujian (No. 2021J05249, 2023J01105), The Guiding Project of Fujian (2023H0021); The Industry-University-Research Cooperation Project of Fujian(2023H6022); Scientific Research Start-up Foundation of Wuyi University (No. YJ202101), the Science and Technology Planning Project of Putian City of Fujian Province (Grant No.:2023GJGZ004). H. C. acknowledges the support from the National Institutes of Health (award Nos. R21EB030140), the National Science Foundation (NSF) (grant Nos. 2309323, 2243979, 2319139, and 2222654), and Penn State University.

Appendix A. Supplementary data

Supplementary data to this article can be found online at https://doi.org/10.1016/j.talanta.2024.126990.

Data availability

No data was used for the research described in the article.

References

[1] V. Katic, P.L. dos Santos, M.F. dos Santos, B.M. Pires, H.C. Loureiro, A.P. Lima, J.C. M. Queiroz, R. Landers, R.A.A. Muñoz, J.A. Bonacin, 3D printed graphene electrodes modified with prussian blue: emerging electrochemical sensing platform for peroxide detection, ACS Appl. Mater. Interfaces 11 (38) (2019) 35068–35078.

[2] R. Goldoni, M. Farronato, S.T. Connelly, G.M. Tartaglia, W.-H. Yeo, Recent advances in graphene-based nanobiosensors for salivary biomarker detection, Biosens. Bioelectron. 171 (2021) 112723.

[3] E. Ferkingstad, P. Sulem, B.A. Atlason, G. Sveinbjornsson, M.I. Magnusson, E. L. Styrmisdottir, K. Gunnarsdottir, A. Helgason, A. Oddsson, B.V. Halldorsson, B. O. Jensson, F. Zink, G.H. Halldorsson, G. Masson, G.A. Arnadottir, H. Katrinardottir, K. Juliusson, M.K. Magnusson, O.T. Magnusson, R. Fridriksdottir, S. Saevarsdottir, S.A. Gudjonsson, S.N. Stacey, S. Rognvaldsson, T. Eiriksdottir, T. A. Olafsdottir, V. Steinthorsdottir, V. Tragante, M.O. Ulfarsson, H. Stefansson, I. Jonsdottir, H. Holm, T. Rafnar, P. Melsted, J. Saemundsdottir, G.L. Norddahl, S. H. Lund, D.F. Gudbjartsson, U. Thorsteinsdottir, K. Stefansson, Large-scale integration of the plasma proteome with genetics and disease, Nat. Genet. 53 (12) (2021) 1712–1721.

[4] R. Ghaffari, D.S. Yang, J. Kim, A. Mansour, J.A. Wright Jr., J.B. Model, D.E. Wright, J.A. Rogers, T.R. Ray, State of sweat: emerging wearable systems for real-time, noninvasive sweat sensing and analytics, ACS Sens. 6 (8) (2021) 2787–2801.

[5] L. Lan, X. Le, H. Dong, J. Xie, Y. Ying, J. Ping, One-step and large-scale fabrication of flexible and wearable humidity sensor based on laser-induced graphene for real-time tracking of plant transpiration at bio-interface, Biosens. Bioelectron. 165 (2020) 112360.

[6] S. Singh, J. Wang, S. Cinti, Review—an overview on recent progress in screen-printed electroanalytical (Bio)Sensors, ECS Sensors Plus 1 (2) (2022) 023401.

[7] H. Yoon, J. Nah, H. Kim, S. Ko, M. Sharifuzzaman, S.C. Barman, X. Xuan, J. Kim, J. Y. Park, A chemically modified laser-induced porous graphene based flexible and ultrasensitive electrochemical biosensor for sweat glucose detection, Sensor. Actuator. B Chem. 311 (2020) 127866.

[8] S. Zhang, A. Chhetry, M.A. Zahed, S. Sharma, C. Park, S. Yoon, J.Y. Park, On-skin ultrathin and stretchable multifunctional sensor for smart healthcare wearables, npj Flexible Electronics 6 (1) (2022) 11.

[9] L. Rotariu, F. Lagarde, N. Jaffrezic-Renault, C. Bala, Electrochemical biosensors for fast detection of food contaminants – trends and perspective, TrAC, Trends Anal. Chem. 79 (2016) 80–87.

[10] Y. Shao, J. Wang, H. Wu, J. Liu, I.A. Aksay, Y. Lin, Graphene based electrochemical sensors and biosensors, A Review 22 (10) (2010) 1027–1036.

[11] A.A. Lahcen, S. Rauf, T. Beduk, C. Durmus, A. Aljedaibi, S. Timur, H.N. Alshareef, A. Amine, O.S. Wolfbeis, K.N. Salama, Electrochemical sensors and biosensors using laser-derived graphene: a comprehensive review, Biosens. Bioelectron. 168 (2020) 112565.

[12] Z. Feng, Z. Geng, S. Pan, Y. Yin, X. Sun, X. Liu, L. Ge, F. Li, In situ patterning of nickel/sulfur-codoped laser-induced graphene electrode for selective electrocatalytic valorization of glycerol, Appl. Catal., B: Environment and Energy 353 (2024) 124101.

[13] C. Zhang, J. Ping, Y. Ying, Evaluation of trans-resveratrol level in grape wine using laser-induced porous graphene-based electrochemical sensor, Sci. Total Environ. 714 (2020) 136687.

[14] C. Jiang, X. Li, Y. Yao, L. Lan, Y. Shao, F. Zhao, Y. Ying, J. Ping, A multifunctional and highly flexible triboelectric nanogenerator based on MXene-enabled porous film integrated with laser-induced graphene electrode, Nano Energy 66 (2019) 104121.

[15] F.M. Vivaldi, A. Dallinger, A. Bonini, N. Poma, L. Sembranti, D. Biagini, P. Salvo, F. Greco, F. Di Francesco, Three-dimensional (3D) laser-induced graphene:

structure, properties, and application to chemical sensing, ACS Appl. Mater. Interfaces 13 (26) (2021) 30245–30260.

[16] L. Huang, J. Su, Y. Song, R. Ye, Laser-induced graphene: en route to smart sensing, Nano-Micro Lett. 12 (1) (2020) 157.

[17] Y. Chen, J. Long, S. Zhou, D. Shi, Y. Huang, X. Chen, J. Gao, N. Zhao, C.-P. Wong, UV laser-induced polyimide-to-graphene conversion: modeling, fabrication, and application, Small Methods 3 (10) (2019) 1900208.

[18] X. Liu, H. Cheng, Y. Zhao, Y. Wang, F. Li, Portable electrochemical biosensor based on laser-induced graphene and MnO2 switch-bridged DNA signal amplification for sensitive detection of pesticide, Biosens. Bioelectron. 199 (2022) 113906.

[19] X. Liu, Y. Wang, Y. Du, J. Zhang, Y. Wang, Y. Xue, J. Zhao, L. Ge, L. Yang, F. Li, Laser-induced graphene (LIG)-based electrochemical microfluidic chip for simultaneous analysis of multiplex microRNAs, Chem. Eng. J. 486 (2024) 150233.

[20] Y. Pan, X. Su, Y. Liu, P. Fan, X. Li, Y. Ying, J. Ping, A laser-engraved wearable electrochemical sensing patch for heat stress precise individual management of horse, Adv. Sci. 11 (28) (2024) 2310069.

[21] G. Xu, Z.A. Jarjes, V. Desprez, P.A. Kilmartin, J. Travas-Sejdic, Sensitive, selective, disposable electrochemical dopamine sensor based on PEDOT-modified laser scribed graphene, Biosens. Bioelectron. 107 (2018) 184–191.

[22] H. Lee, S.M. Dellatore, W.M. Miller, P.B. Messersmith, Mussel-inspired surface chemistry for multifunctional coatings, Science 318 (5849) (2007) 426–430.

[23] Q. Ye, F. Zhou, W. Liu, Bioinspired catecholic chemistry for surface modification, Chem. Soc. Rev. 40 (7) (2011) 4244–4258.

[24] S. Daboss, J. Lin, M. Godejohann, C. Kranz, Redox switchable polydopamine-modified AFM-SECM probes: a probe for electrochemical force spectroscopy, Anal. Chem. 92 (12) (2020) 8404–8413.

[25] D. Aguilar-Ferrer, J. Szewczyk, E. Coy, Recent developments in polydopamine-based photocatalytic nanocomposites for energy production: physico-chemical properties and perspectives, Catal. Today 397–399 (2022) 316–349.

[26] E. Chalmers, H. Lee, C. Zhu, X. Liu, Increasing the conductivity and adhesion of polypyrrole hydrogels with electropolymerized polydopamine, Chem. Mater. 32 (1) (2020) 234–244.

[27] J. Saiz-Poseu, J. Mancebo-Aracil, F. Nador, F. Busqué, D. Ruiz-Molina, The chemistry behind catechol-based adhesion, Angew. Chem. Int. Ed. 58 (3) (2019) 696–714.

[28] M. Bonora, S. Patergnani, A. Rimessi, E. De Marchi, J.M. Suski, A. Bononi, C. Giorgi, S. Marchi, S. Missiroli, F. Poletti, M.R. Wieckowski, P. Pinton, ATP synthesis and storage, Purinergic Signal. 8 (3) (2012) 343–357.

[29] J.A. Smeitink, M. Zeviani, D.M. Turnbull, H.T. Jacobs, Mitochondrial medicine: a metabolic perspective on the pathology of oxidative phosphorylation disorders, Cell Metabol. 3 (1) (2006) 9–13.

[30] A.W. Boots, G.R.M.M. Haenen, G.J.M. den Hartog, A. Bast, Oxidative damage shifts from lipid peroxidation to thiol arylation by catechol-containing antioxidants, Biochim. Biophys. Acta Mol. Cell Biol. Lipids 1583 (3) (2002) 279–284.

[31] P. Parkkila, T. Viitala, Partitioning of catechol derivatives in lipid membranes: implications for substrate specificity to catechol-O-methyltransferase, ACS Chem. Neurosci. 11 (6) (2020) 969–978.

[32] J.H. Lee, J.S. Ryu, Y.K. Kang, H. Lee, H.J. Chung, Polydopamine sensors of bacterial hypoxia via fluorescence coupling, Adv. Funct. Mater. 31 (9) (2021) 2007993.

[33] E. Grignon, S.Y. An, A.M. Battaglia, D.S. Seferos, Catechol homopolymers and networks through postpolymerization modification, Macromolecules 55 (22) (2022) 10167–10175.

[34] B. Stöckle, D.Y.W. Ng, C. Meier, T. Paust, F. Bischoff, T. Diemant, R.J. Behm, K.-E. Gottschalk, U. Ziener, T. Weil, Precise control of polydopamine film formation by electropolymerization, Macromol. Symp. 346 (1) (2014) 73–81.

[35] A. Olejnik, M. Ficek, M. Szkodo, A. Stanisławska, J. Karczewski, J. Ryl, A. Dołęga, K. Siuzdak, R. Bogdanowicz, Tailoring diffusional fields in zwitterion/dopamine copolymer electropolymerized at carbon nanowalls for sensitive recognition of neurotransmitters, ACS Nano 16 (8) (2022) 13183–13198.

[36] W. Guo, H. Xu, C. Chen, X. Cao, J. Ma, Y. Liu, Determination of U(VI) by differential pulse stripping voltammetry using a polydopamine/reduced graphene oxide nanocomposite modified glassy carbon electrode, Microchem. J. 175 (2022) 107111.

[37] D.R. Kumar, S. Kesavan, T.T. Nguyen, J. Hwang, C. Lamiel, J.-J. Shim, Polydopamine@electrochemically reduced graphene oxide-modified electrode for electrochemical detection of free-chlorine, Sensor. Actuator. B Chem. 240 (2017) 818–828.

[38] J. Szewczyk, D. Aguilar-Ferrer, E. Coy, Polydopamine films: electrochemical growth and sensing applications, Eur. Polym. J. 174 (2022) 111346.

[39] H. Guo, A simple algorithm for fitting a Gaussian function [DSP tips and tricks], IEEE Signal Process. Mag. 28 (5) (2011) 134–137.

[40] T. Lu, F. Chen, Multiwfn: a multifunctional wavefunction analyzer, J. Comput. Chem. 33 (5) (2012) 580–592.

[41] J. Liebscher, R. Mrówczyński, H.A. Scheidt, C. Filip, N.D. Hădade, R. Turcu, A. Bende, S. Beck, Structure of polydopamine: a never-ending story? Langmuir 29 (33) (2013) 10539–10548.

[42] H. Coskun, A. Aljabour, T. Greunz, M. Kehrer, D. Stifter, P. Stadler, Electrochemical hydrogen storage in amine-activated polydopamine, Advanced Sustainable Systems 5 (1) (2021) 2000176.

[43] S. Chumillas, T. Palomäki, M. Zhang, T. Laurila, V. Climent, J.M. Feliu, Analysis of catechol, 4-methylcatechol and dopamine electrochemical reactions on different substrate materials and pH conditions, Electrochim. Acta 292 (2018) 309–321.

[44] Y. Wang, Y. Jia, Y. Zhou, Y. Wang, G. Zheng, K. Dai, C. Liu, C. Shen, Ultra-stretchable, sensitive and durable strain sensors based on polydopamine encapsulated carbon nanotubes/elastic bands, J. Mater. Chem. C 6 (30) (2018) 8160–8170.

[45] K. Muzyka, G. Xu, Laser-induced graphene in facts, numbers, and notes in view of electroanalytical applications: a review, Electroanalysis 34 (4) (2022) 574–589.

[46] J. Zanoni, J.P. Moura, N.F. Santos, A.F. Carvalho, A.J.S. Fernandes, T. Monteiro, F. M. Costa, S.O. Pereira, J. Rodrigues, Dual transduction of H2O2 detection using ZnO/Laser-Induced graphene composites, Chemosensors (2021).

[47] M. Amiri, E. Amali, A. Nematollahzadeh, Poly-dopamine thin film for voltammetric sensing of atenolol, Sensor. Actuator. B Chem. 216 (2015) 551–557.

[48] X. Li, C. Wu, B. Hou, J. Wu, R. Sun, M. Chen, Molecular investigation of interplay mechanism between polydopamine and graphene oxide: the effect of oxidation degree on the adsorption behavior of polydopamine, Appl. Surf. Sci. 611 (2023) 155759.

[49] A.J. Bard, L.R. Faulkner, H.S. White, Electrochemical Methods: Fundamentals and Applications, John Wiley & Sons, 2022.

[50] M. Pandurangachar, B.E.K. Swamy, O. Gilbert, B.S. Sherigara, U. Chandra, Simultaneous determination of dopamine, ascorbic acid and uric acid at poly (patton and reeder's) modified carbon paste electrode, Int. J. Electrochem. Sci. 4 (5) (2009) 672–683.

[51] S.J. Konopka, B. McDuffie, Diffusion coefficients of ferri- and ferrocyanide ions in aqueous media, using twin-electrode thin-layer electrochemistry, Anal. Chem. 42 (14) (1970) 1741–1746.

[52] M. Behpour, E. Honarmand, S.J.B.o.t.K.C.S. Ghoreishi, Nanogold-modified carbon paste electrode for the determination of atenolol in pharmaceutical formulations and urine by voltammetric methods, Bull. Korean Chem. Soc. 31 (4) (2010) 845–849.

[53] A. Chen, B. Shah, Electrochemical sensing and biosensing based on square wave voltammetry, Anal. Methods 5 (9) (2013) 2158–2173.

[54] M.A. Haque, K. Morozova, G. Ferrentino, M. Scampicchio, Electrochemical methods to evaluate the antioxidant activity and capacity of foods: a review, Electroanalysis 33 (6) (2021) 1419–1435.